Grain boundary susceptibility to liquid metal embrittlement during wire arc additive manufacturing of a bronze/stainless steel bimetallic structure

Mahmoudiniya, Mahdi; Hermans, Marcel J.M.; Kestens, Leo A.I.

DOI
10.1016/j.matchar.2025.115058

Publication date
2025

Document Version
Final published version

Published in
Materials Characterization

Materials Characterization 224 (2025) 115058

Contents lists available at ScienceDirect

Materials Characterization

journal homepage: www.elsevier.com/locate/matchar

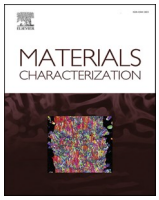

Grain boundary susceptibility to liquid metal embrittlement during wire arc additive manufacturing of a bronze/stainless steel bimetallic structure☆

Mahdi Mahmoudiniya [a,*], Marcel J.M. Hermans [b], Leo A.I. Kestens [a,b]

[a] Ghent University, Metals Science and Technology Group, Technologiepark 903 B-9052 Zwijnaarde, Ghent, Belgium
[b] Delft University of Technology, Department of Materials Science and Engineering, Mekelweg, 22628 CD Delft, the Netherlands

ARTICLE INFO

Keywords:
Liquid metal embrittlement
Additive manufacturing
Crack propagation
Grain boundaries

ABSTRACT

In the present study, the crystallography aspects of the liquid metal embrittlement (LME) phenomenon are investigated in a bi-metallic bronze-stainless steel structure, produced using wire arc additive manufacturing. Most of the LME cracks were found to be propagated along high-angle grain boundaries of the austenitic structure. Surprisingly, it was observed that in some cases, LME cracks propagated transgranularly in austenite grains, which is a rare phenomenon in LME of steels. The Σ3-coincidence site lattice (CLS) boundaries showed the highest resistance to LME compared to other CLS types. It was also found that the presence of elongated grains in additively manufactured microstructures can accelerate the LME phenomenon.

1. Introduction

Liquid metal embrittlement (LME) is a phenomenon that occurs when a ductile metal is exposed to a liquid metal, leading to a reduction in its ductility. During the LME, the aggressive liquid metal attacks a susceptible solid metal, and under tensile stresses, cracks are initiated and propagate along the grain boundaries, leading to loss of ductility [1]. One example of LME is the embrittling of some steels by copper-based alloys. This LME is also known as "*copper contamination cracking*", observed in the heat-affected zone (HAZ) of welds in certain steels [2] [3]. The source of the copper resulting in LME in the Cu—Fe couple can be attributed to welding fixtures, the contact tube of the wire feeding system and shielding gas nozzle, or copper tooling. These parts are mostly made of copper or its alloys because of their high thermal conductivity. In the HAZ, where the temperature is higher than the melting point of the copper (1083 °C), the copper wets the surface of the steel and penetrates the grain boundaries of the HAZ microstructure, which is typically in the austenitic phase. In the past, the LME in the Cu—Fe couple has also been reported for different processes, e.g., the surfacing process of steels with copper alloy, the brazing of steels using copper fillers and welding of copper or its alloys to steels [4].

With the emergence of additive manufacturing techniques to produce multi-material constructs, the issue of LME has been raised again, when copper alloys need to be printed on a steel substrate and a molten copper-based alloy is in contact with the solid steel, while stresses are induced in the construct by the nature of the printing process. Raghavendra et al. [5] reported the formation of LME cracks during laser-powder direct energy deposition of CuSn10 alloy on a 42CrMo4V martensitic steel substrate. However, they did not discuss the microstructure developed at the interface nor the mechanisms of crack formation. Kuai et al. [6] also found LME cracks at the interface of a 316 L/CuCrZr bi-metallic structure manufactured using the laser powder bed fusion (LPBF) technique. Dharmendra et al. [3,4] observed LME cracks during bronze deposition on AISI 316 stainless steel using wire arc additive manufacturing (WAAM).

Different models that have been proposed for LME, all involve physical or chemical reactions between liquid metal atoms and solid atoms at the tip of the crack. Considering the occurrence of these reactions and crack propagation along the grain boundaries, regardless of the mechanisms, it appears that grain boundary characteristics are important in LME cracking. In the case of embrittling aluminium with gallium, it has been shown that low-angle grain boundaries are penetrated more slowly than high-angle grain boundaries [7]. It has also been revealed that, in the case of coincidence site lattice (CSL) boundaries, low Σ boundaries have significantly higher LME resistance than high Σ CSL boundaries [7]. Razmpoosh et al. [8] also found that in the Zn-Fe(FCC) couple, low-energy Σ boundaries can suppress the LME. To the best of the author's knowledge, no reports have been published yet

☆ This article is part of a Special issue entitled: 'ICOTOM' published in Materials Characterization.

* Corresponding author.
E-mail address: mahdi.mahmoudiniya@Ugent.be (M. Mahmoudiniya).

https://doi.org/10.1016/j.matchar.2025.115058
Received 26 February 2025; Received in revised form 14 April 2025; Accepted 15 April 2025
Available online 16 April 2025

on the effect of grain and grain boundaries on the LME in the Cu—Fe couple. An innovative aspect of this study lies in its focus on 3D printing, distinguishing it from most previous research on LME, which has predominantly been conducted in the context of welding or coating processes. Accordingly, this study focuses on the properties of the grain and grain boundaries affected by LME during WAAM of the bi-metallic component composed of nickel aluminium bronze deposited on martensitic stainless steel.

2. Materials and methods

The WAAM technique was employed to 3D print the bimetallic structure in this study. A martensitic steel (AISI 410) component with dimensions of 200 mm, 30 mm and 30 mm (for length, width, and height, respectively) was printed in a linear bi-direction manner using a 1.2 mm diameter wire. On top of the martensite steel substrate, the bronze alloy (Cu 6327) was deposited in a weaving pattern, also using a 1.2 mm diameter wire, with a height of 20 mm. The chemical composition of the wires utilized is summarized in Table 1.

Table 2 presents the details of the printed parameters for both parts.

To assess the LME phenomenon at the interface, the printed part was sectioned perpendicular to the welding direction of the steel part and analyzed using Optical Microscopy (OM), Scanning Electron Microscopy (SEM) and Electron Backscatter Diffraction (EBSD). The samples were prepared for OM and SEM analysis following standard metallographic procedures, including grinding, polishing, and etching with Vilella's reagent. For EBSD measurements, an additional polishing step using OPS solution was performed. The EBSD measurements were conducted under a 20 kV gun voltage, with a beam spot size of 5 nm, with a hexagonal grid with a step size ranging from 50 to 100 nm. The collected data was then processed using OIM analysis software version 9. A substantial dataset of over 1700 grains was gathered from ten different LME cracks, and the various characteristics of these grains were analyzed. In addition, more than 4000 paired points along the cracks were manually collected to analyze the misorientation information along the crack path.

3. Results

Figure 1 shows the interface of the printed bimetallic structure, where some cracks are observed in the HAZ of the steel part. One of the distinctive features of LME, setting it apart from other types of cracking, such as thermal stress cracking, is the presence of solidified liquid within the cracks. This is clearly visible in the backscattered electron (BSE) images in Fig. 1.

Fig. 2 provides detailed insights into the microstructure surrounding an LME crack through simultaneous EDS and EBSD analysis. This combined technique is highly effective in distinguishing LME cracks from other potential crack types, as LME cracks are always filled with penetrated and solidified alloy that is detectable via EDS.

The microstructure surrounding the crack exhibits a martensitic structure with a lath morphology, as shown in Fig. 2a. Phase analysis and the Cu distribution map, illustrated in Fig. 2b and c, reveal that an alloy with a distinct crystallographic structure and chemical composition has solidified within the crack. The formation of a martensitic structure is logically anticipated during the WAAM by means of Gas Metal Arc welding of 410 stainless steel as cooling rates are fairly high and has also been reported by various researchers [9–12]. To gain a deeper understanding of the LME phenomenon in the couple of NiAl bronze (NAB) – AISI 410 stainless steel, examining phase stability during this process is of importance. Fig. 3 shows equilibrium phase diagrams calculated by Thermo-Calc software for NAB alloy and 410 stainless steel. As it is seen, the NAB alloy solidifies between 1050 and 1030 °C (cf. Fig. 3a), where the stainless steel has an austenitic structure in this range of temperature (cf. Fig. 3b), implying that LME is likely to occur in the austenite phase. Accordingly, to study the crack path of the LME in the current case, the initial austenite phase was reconstructed using OIM software from the martensite structure based on the Greninger and Troiano (G–T) orientation relationship, as shown in Fig. 2d. The selection of the G–T orientation relationship was based on an assessment of the retained austenite boundaries in relation to the surrounding martensite, where this relationship appeared to be the most evident.

In total, ten LME cracks were analyzed and Table 3 presents a summary of the results of the misorientation analysis of non-LME affected regions and of selected paired points along the LME crack paths, whereby each point of the pair is on either side of the crack. It is notable that in the present study, the GBs are divided based on their misorientation angle into three groups: 1) low-angle grain boundaries (LAGB) with a misorientation angle lower than 15°, 2) random high-angle grain boundaries (R-HAGB) with a misorientation angle higher than 15° and with a random structure, 3) High-angle grain boundaries with CSL characteristic (CSL). To determine whether a boundary qualifies as a CSL boundary, a tolerance angle is applied, defined by the formula $D = K/\Sigma^n$, which is known as Brandon's criterion. The Common values of $K = 15^\circ$ and $n = 1/2$ were used in the present study.

If the data are normalized with respect to the random non-cracked base material, it can be observed that the crack (i) primarily runs along HAGBs, (ii) avoids LAGBS, and (iii) is slightly depleted from CSL boundaries. Analyzing the crack path shows that most of the cracks (more than 96.3 %) propagate along HAGBs in the prior austenite microstructure. However, 3.7 % of LAGBs were along the crack path, which is surprising for a failure phenomenon known to be intergranular. The fraction of LAGBs along the crack path (3.7 %) is lower than its fraction along uncracked boundaries (7.6 %). This suggests that although there are statistically more LAGBs in the vicinity of the crack than along the crack path, the crack prefers to propagate along the HAGBs. Fig. 4a shows the distribution of misorientation angle along the crack path and also in the uncracked microstructure. It is seen that most of the HAGBs which are sensitive to LME have misorientation angles of ~30–55°.

Analyzing the grain boundaries of the uncracked austenitic microstructure shows that 17.6 % of grain boundaries are CSL boundaries. However, for the cracked boundaries, 15.5 % of the crack propagations occur through CSL boundaries. Fig. 4b compares the distribution of CSL boundaries in uncracked and cracked boundaries. It should be noted that CSL boundaries with Σ values greater than 29 are considered random high-angle boundaries and are not included in our analysis. For the uncracked microstructure, the observed CSL boundaries were mainly Σ3, Σ5, Σ9 and Σ11, and the rest of the CSL boundaries had fractions lower than 1 %. For the crack path, the Σ3, Σ5, and Σ9 types of CSL boundaries are the main ones. Comparing the fraction of CSL boundaries in uncracked and cracked boundaries shows that the main difference is related to the Σ3 boundary: 3.6 % in uncracked boundaries and 2.1 % in cracked boundaries. It shows that Σ3-CSL boundaries have the highest resistance among CSL boundaries to copper-LME. Razmpush et al. [8] also showed that increasing the fraction of special CSL boundaries in the microstructure of 304 austenitic stainless steel significantly improves the resistance against LME with Zn.

Table 1
Chemical composition (wt%) of the used wires to print the bimetallic structure.

	C	Si	Mn	Ni	Cr	Mo	Fe	Cu	Al
AM 410NiMo	0.01	0.65	0.7	4.8	12.2	0.5	Bal	<0.1	_
AM Cu6327	_	_	1.8	2.5	_	_	1.3	Bal	8.6

Table 2
Printing parameters fabricate the bi-metallic structure.

	Arc current (A)	Arc voltage (V)	Travelling speed (mm/min)	Shield gas flow rate (l/min)	Layer thickness (mm)	Hatch distance (mm)
410 steel	222	17.2	650	15	3	5
Bronze alloy	212	22	1500–2500	18	1.5	–

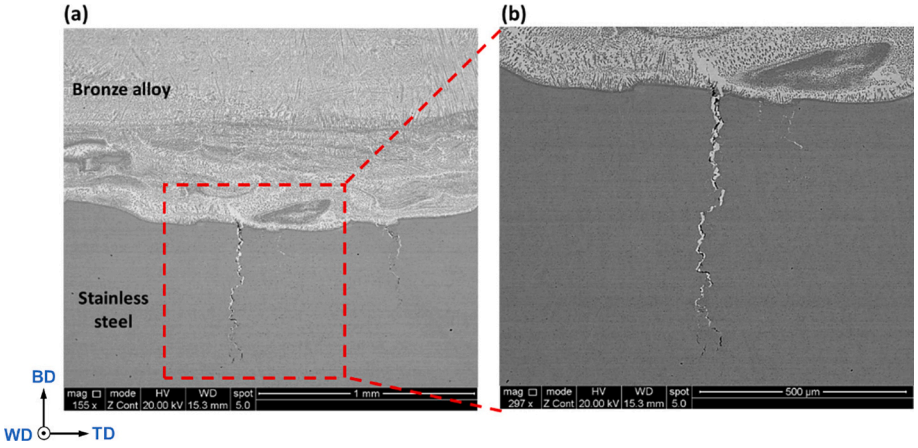

Fig. 1. BSE images of formed cracks at the interface of bronze and stainless steel.

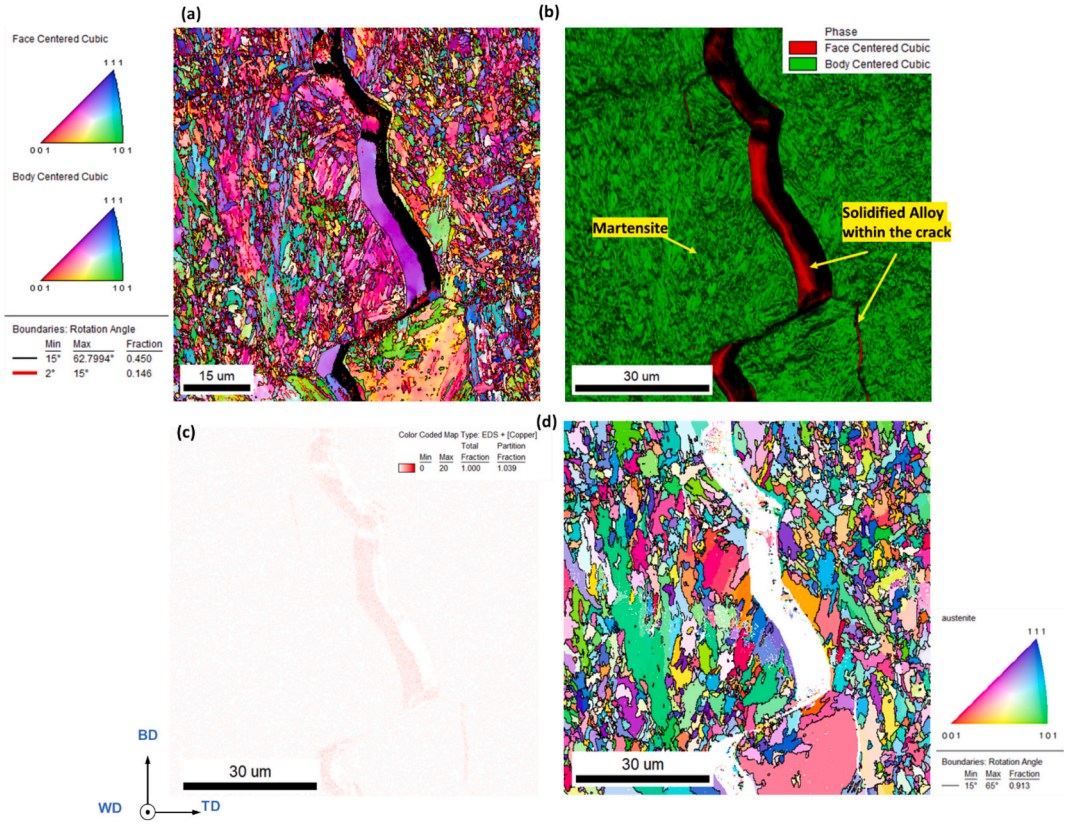

Fig. 2. A typical result of simultaneous EBSD + EDS measurements of an LME crack propagated in steel (a): BD-IPF, (b): Phase map, (c): distribution map of the copper and (d): BD-IPF of the reconstructed austenite phase.

In addition to the misorientation angle, the rotation axis of the misorientation data was also analyzed, as shown in Fig. 5.

A comparison of the distribution of the rotation axis of misorientation for crack paths and boundaries in an uncracked microstructure shows that the rotation axis for the grain boundaries within the crack paths is close to ⟨111⟩, while for the boundaries of uncracked microstructure are <111> and ⟨101⟩.

The EBSD data was also used to calculate the Schmid Factor (SF) for individual grains by analyzing their crystallographic orientations. The SF is an important metric that relates to the ease in which a grain can

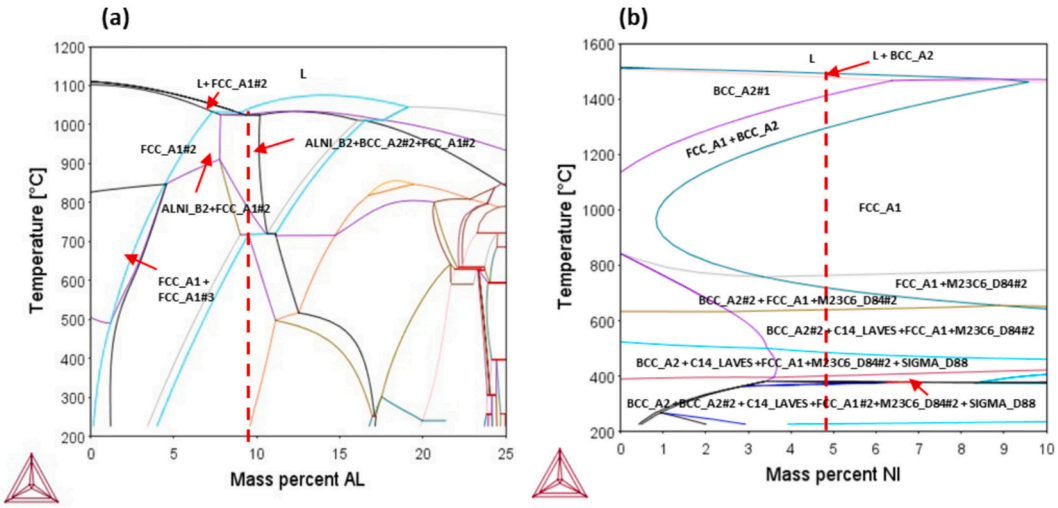

Fig. 3. Phase diagrams of (a) NAB alloy and (b) 410 stainless steel calculated by Thermo-Calc.

Table 3
Comparison of the grain boundary characteristics along the cracked and uncracked boundaries.

		Cracked boundaries	Uncracked boundaries
HAGB	LAGB %	3.7	7.6
	Random -HAGB %	80.8	74.8
	CSL %	15.5	17.6

deform plastically under a given stress state. The grains with higher SF are more likely to accommodate deformation easily, leading to higher local stresses that can contribute to crack formation and growth. In this context, all grains in contact with the LME cracks were manually selected and analyzed, then compared with those not in contact with the cracks. To calculate the SF, it is essential to consider the stress conditions present when the LME occurs after the deposition of the final stainless steel layer. Since the deposition of bronze layers alters the stress state in the final printed part, measuring residual stresses at the last deposited layer of steel after printing the complete part may not provide an accurate representation and could be misleading. Moat et al. [13] analyzed residual stress conditions during the direct energy deposition of a Waspaloy using neutron measurements and modelling. Their results indicated that at the mid-length of the deposited wall's top layer, the BD (Build Direction) and TD (Transverse Direction) stresses are close to zero, while tensile stresses were observed in the WD (welding Direction). This approach was used in the present study to calculate the Schmid factor, ensuring a more accurate assessment of the stress state under LME conditions. The average SF for grains in contact with the crack and those not in contact was 0.47 and 0.46, respectively. Although the average SF value is similar for both cracked grains and the rest of the microstructure, their distribution differs, as illustrated in Fig. 6.

Analysis of the SF distribution reveals that a higher fraction of grains in contact with the LME cracks have a high SF (>0.4) compared to grains not in contact with the cracks, at 91 % versus 86 %, respectively. In addition, sharp peaks are observed in the SF distribution for grains in contact with the LME cracks, particularly in the range of 0.4 to 0.5. The size and shape of grains near the LME cracks were also analyzed using EBSD data, and the results were compared with those of the entire microstructure, as shown in Fig. 7.

The average grain size for grains in contact with the crack was 16.8 ± 15.46 μm, whereas for the entire microstructure, it was 5.07 ± 4.6 μm. Grain shape was quantified by the aspect ratio, which is defined as the ratio of the minor axis length to the major axis length. Grains with an aspect ratio above 0.33 were classified as equiaxed, while those below this threshold were classified as columnar. In the overall microstructure of parent austenite, 71 % of the grains were equiaxed, with the remaining 29 % exhibiting a columnar morphology. In contrast, among the grains in contact with the crack path, 58 % showed an equiaxed morphology, while 42 % exhibited a columnar shape. It means that the LME cracks tend to propagate along large and elongated grains of

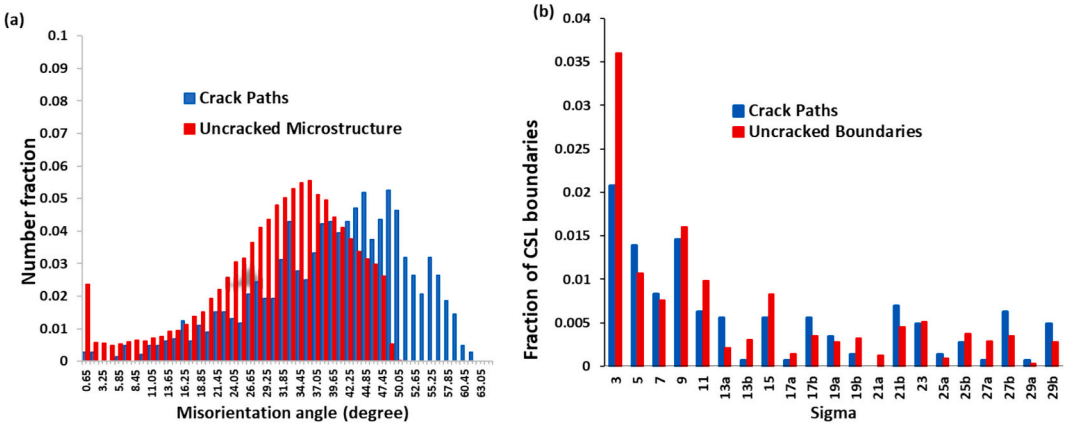

Fig. 4. (a) The distribution of misorientation angle for cracked and uncracked boundaries, (b): fraction of different CSL boundaries for crack paths and uncracked boundaries.

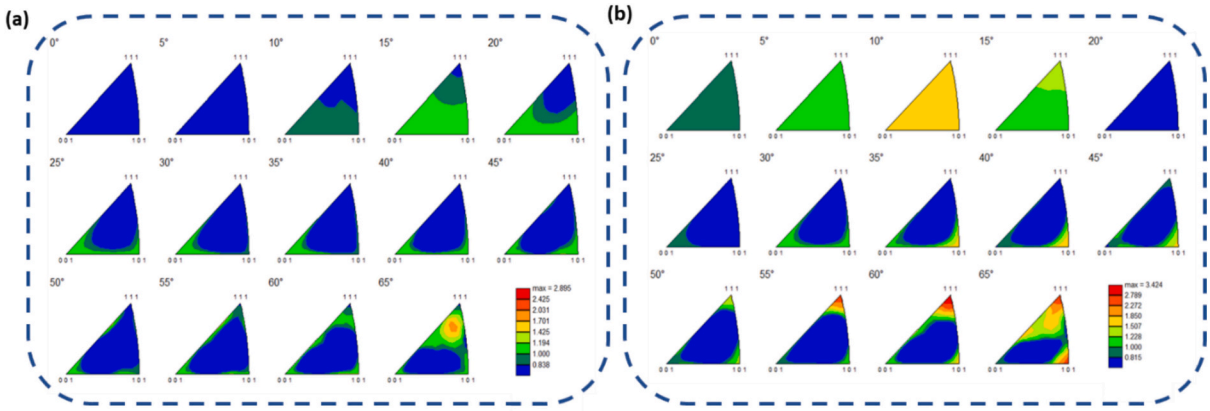

Fig. 5. Axis/angle misorientation distribution of (a) the crack paths and (b) the uncracked microstructure.

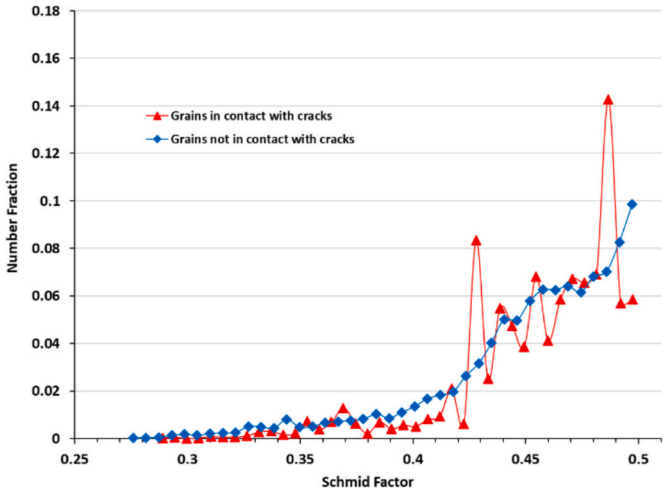

Fig. 6. Distribution of SF for grains in and not in contact with the LME cracks.

austenite rather than small and equiaxed grains. The distributions of the major and minor axes of the grains further indicate that grains in contact with the cracks have wider ranges than those in the unaffected microstructure, confirming that these grains have larger dimensions, consistent with grain size measurements. The results are summarized in Table 4.

4. Discussion

Analyzing the misorientation data along the crack path showed that 3.7 % of the crack boundaries are LAGBs. This means that this fraction of points on both sides of the crack have identical orientations or the misorientation is lower than 15°, a criterion used for grain definition that translates to transgranular cracking of parent austenite during LME. Fig. 8 shows some of these grains.

The same orientations of the pair point across the crack in the IPF map, c.f. Fig. 8c proves the transgranular nature of the crack in some regions. Noticeably, having the same color in one IPF map does not necessarily mean having the same crystal orientation. For example, in Fig. 8c, two grains across the crack marked by a yellow dashed oval have the same color across the crack but show a misorientation angle of 41 degrees. To the best of the authors' knowledge, the LME generated by copper alloys in steels is reported to propagate exclusively intergranularly [14–19]. Even for the LME of steels by other liquid metals, there are only a few reports on transgranular cracking. In this context, Barkia et al. [20] reported the transgranular cleavage fracture of austenite during sodium-assisted LME in 304 austenitic steel. There is another research about transgranular cracking of grains because of Zn-assisted LME [21] when the steel has a dual phase structure of ferrite and austenite at the temperature that LME happens. However, they only observed this transgranular cracking behavior in ferritic grains. Accordingly, the current research is the only one that observes the transgranular cracking of austenite grains in Cu-assisted LME of steels. The trace analysis indicates that transgranular fracture occurs on the {100} and {111} planes in austenite, c.f. Fig. 8d and e. Barika et al. [20] also reported cleavage fractures on the {100} plane during sodium-assisted LME in 304 austenitic stainless steel. Such cleavage fractures are uncommon in face-centered cubic (FCC) structures, as plastic deformation typically precedes cleavage fracture. However, it can occur at very low temperatures when the primary slip systems are inactive, which is not the case here. This transgranular cleavage behavior is likely explainable with the "adsorption-induced cohesion reduction" theory proposed for LME. Based on this model, the adsorption of liquid metal atoms can influence the electronic structure of atoms at the crack tip, reducing the metallic atomic bond strength. In the present case, the copper adsorption reduces the cleavage stress of austenite and promotes transgranular fracture [1]. In this context, the work of Legris et al. [22] has shown that the adsorption of liquid atoms like Bi by pure iron can reduce the surface energy of {001}, {011} and {111} planes by 28, 39 and 18 %, respectively.

The fact that cracks propagate more along R-HAGBs is due to the higher energy of these boundaries than LAGBs or CLS boundaries, which reduces the required stress triggering LME. Analysis of the CSL boundaries indicated that Σ3 boundaries exhibit the highest resistance to LME, cf. Fig. 4b. While limited data exist on the Fe (FCC)-Cu LME system, findings from other LME couples provide useful insights. Razmpoosh et al. [23] also reported that Σ3-CSL boundaries resist LME in various systems, such as Fe (BCC)-Zn, even under maximum stress conditions. The higher resistance of the Σ3-CSL boundaries is related to their low energy compared to random high-angle grain boundaries. Their lower energy is due to high atomic alignment and symmetry, resulting in a well-ordered structure. This well-ordered structure reduces the excess volume of the boundary, which translates to fewer defects or open sites in the boundary that improve the immunity against chemical and physical reactions [24] associated with LME. In the Al—Ga couple, studies have shown that boundaries with the lowest excess volume exhibit slower penetration rates, while boundaries with relatively high excess volume are penetrated more quickly [7]. It is noticeable that even a low fraction of such immune boundaries is important as they disrupt the continuity of susceptible high-angle grain boundaries. This is because the connectivity of boundary types governs grain boundary transport-related properties. So, disrupting continuous pathways formed by connected random boundaries within the microstructure plays a critical role in this context.

Grains with high SF are more favorably oriented for slip under

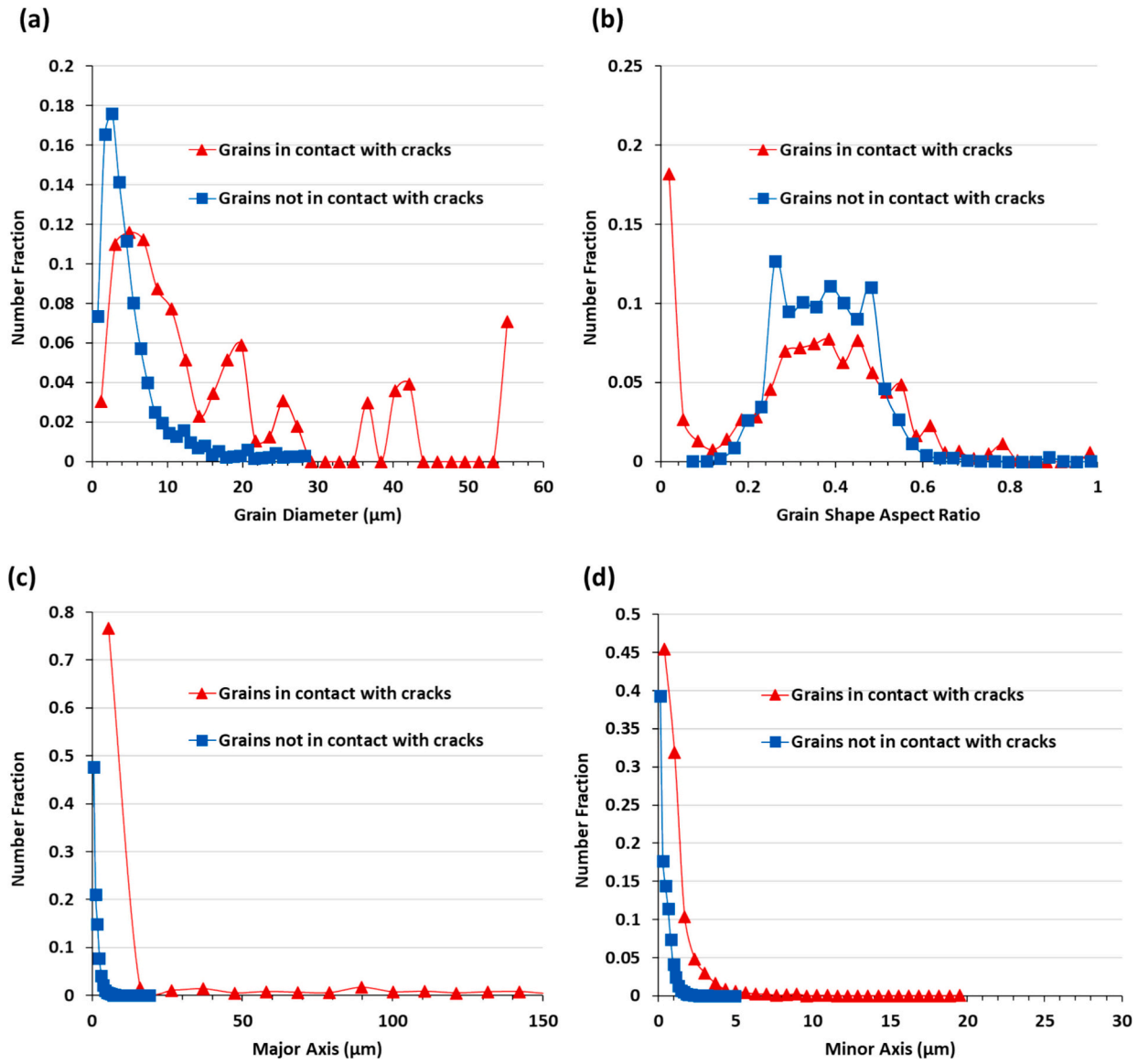

Fig. 7. The results of analyzing the shape and size of the grains in contact and not in contact with the cracks.

Table 4
Comparison of grain size and morphology for grains in contact with LME cracks and the uncracked microstructure.

	Grain size (μm)	Aspect ratio	Major axis (μm)	Minor axis (μm)
Grains in contact with the LME cracks	16.88 ± 15.46	0.15 ± 0.09	108.7 ± 96.1	5.1 ± 4.8
Uncracked microstructure	5.067 ± 4.63	0.529 ± 0.28	9.554 ± 5.589	2.556 ± 1.46

applied stress, which results in more significant plastic deformation and the development of localized stress concentrations, making these grains more prone to cracking. The tendency of grains with SF above 0.4, Fig. 6, being in contact with cracks suggests that the resolved shear stress in these grains often exceeds the material's local strength. Moreover, stress and strain incompatibility between neighboring grains further exacerbate the issue: grains with different SF deform unevenly, creating strain incompatibilities at their boundaries, leading to stress concentrations that promote crack initiation.

The size and shape of grains also play an important role in crack propagation behavior during LME cracking. In this context, Price et al. [25] have shown that the embrittlement of Monel 400 alloy in contact with liquid mercury decreases in severity with a reduction in grain size. In the present study, it was observed that large and elongated grains tend to promote crack propagation, while refined equiaxed grains offer better resistance to crack growth, cf. Fig. 7 and Table 4. In elongated grains, cracks can propagate more easily along the grain boundaries due to the continuous and aligned structure. This provides a straight path, allowing the crack to move with less resistance and accelerating crack propagation. In contrast, in refined equiaxed grains, cracks encounter more grain boundaries in different orientations, causing them to change direction frequently. This zig-zag path requires additional energy and slows down the crack propagation, thus making the microstructure more resistant to fracture. The presence of a high fraction of elongated grains in the microstructure is due to the nature of the additive manufacturing process, where most of the grains in melt pools have an elongated morphology. This can emphasize the post-heat treatment's importance in altering the morphology and grain size of the as-built microstructure.

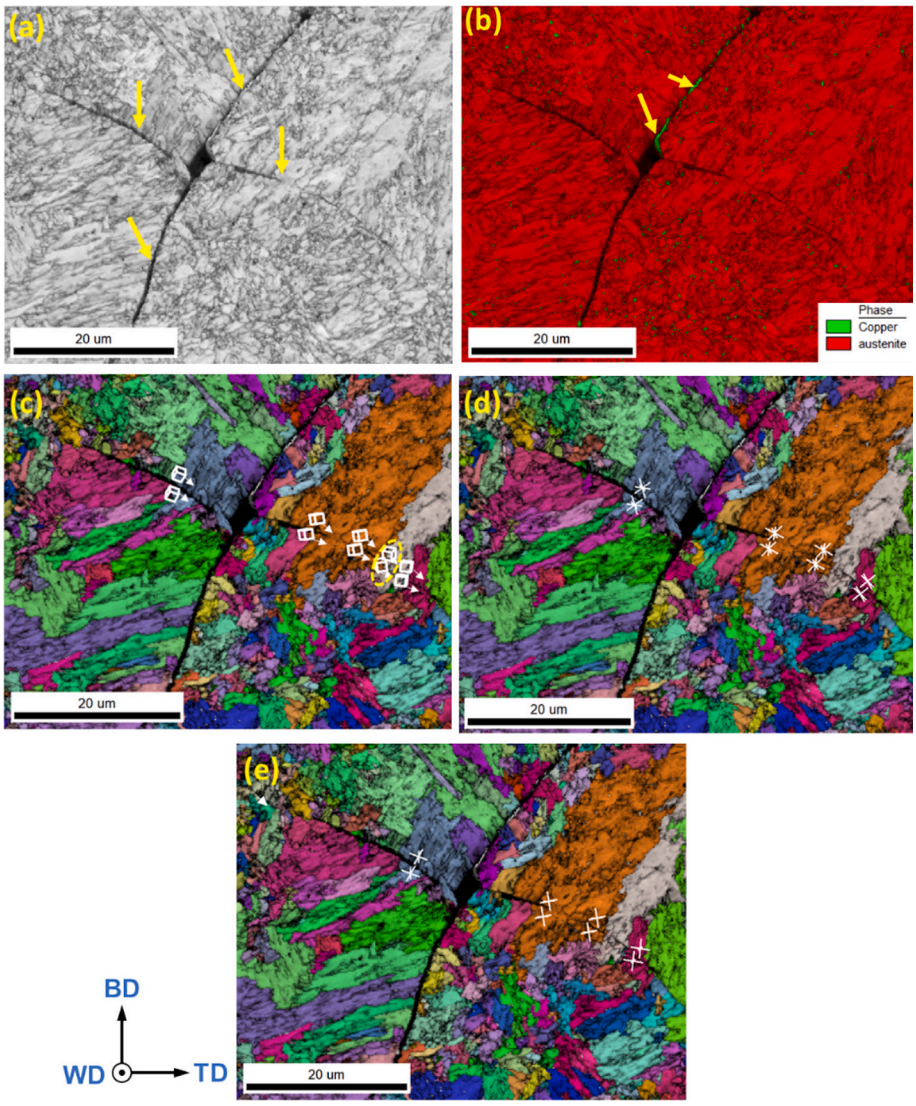

Fig. 8. Transgranular cracking during LME (a): Image quality map (arrows showing the cracks), (b): the phase map (arrows showing the presence of copper alloy within the crack), (c): BD-IPF of parent austenite showing grains at two sides of cracks with the same orientation, (d) and (e): the trace analysis of {100} and {111} planes, respectively, for transgranulary cracked grains.

5. Conclusions

The current study investigated the crystallography aspects of LME in the Fe(FCC)-Cu system during the production of a bimetallic structure of bronze-stainless steel using wire arc additive manufacturing. The main conclusions can be summarized as follows:

- Although most LME cracks (more than 96.3 %) propagate along the HAGBs in the prior austenite structure, in some cases, the cracks are transgranular, which is surprising for LME being an intergranular failure phenomenon, at least for systems including steels.
- Among different CLS boundaries, the Σ3-CLS type showed the highest resistance to LME.
- It was observed that large and elongated grains developed during additive manufacturing tend to promote crack propagation, while refined equiaxed grains offer greater resistance to crack growth.

CRediT authorship contribution statement

Mahdi Mahmoudiniya: Writing – original draft, Validation, Methodology, Investigation, Formal analysis, Conceptualization. **Marcel J. M. Hermans:** Writing – review & editing, Visualization, Supervision, Resources, Project administration, Conceptualization. **Leo A.I. Kestens:** Writing – review & editing, Visualization, Validation, Supervision, Resources, Project administration, Methodology, Funding acquisition.

Declaration of competing interest

The authors declare that they have no known competing financial interests or personal relationships that could have appeared to influence the work reported in this paper.

Acknowledgement

This research was carried out within the project “Grade2XL - Functionally Graded Materials for Extra Large Structures”, which was funded by the European Union’s Horizon 2020 research and innovation program under grant agreement No 862017.

Data availability

The data necessary to replicate these results cannot be shared

currently as it is part of an ongoing study. However, the authors are open to sharing any particular data on request.

References

[1] M.H. Razmpoosh, C. DiGiovanni, Y.N. Zhou, E. Biro, Pathway to understand liquid metal embrittlement (LME) in Fe-Zn couple: from fundamentals toward application, Prog. Mater. Sci. 121 (2021) 100798, https://doi.org/10.1016/j.pmatsci.2021.100798.

[2] C. Heiple, W. Bennett, T. Rising, Embrittlement of several stainless steels by liquid copper and liquid braze alloys, Mater. Sci. Eng. 52 (1982) 277–289, https://doi.org/10.1016/0025-5416(82)90157-4.

[3] W.F. Savage, E.F. Nippes, R.P. Stanton, Intergranular attack of steel by molten copper, Weld, Res. Suppl. 57 (1978) 9–16.

[4] J.C. Lippold, Welding Metallurgy and Weldability, 2014.

[5] S. Raghavendra, P. Jayashree, D.A. Rita, G. Piras, D. Scheider, M. Chemello, M. Benedetti, Wear and material characterization of CuSn10 additively manufactured using directed energy deposition, Add. Manufact. Lett. 6 (2023) 100136, https://doi.org/10.1016/j.addlet.2023.100136.

[6] Z. Kuai, Z. Li, B. Liu, Y. Chen, H. Li, P. Bai, Microstructure and mechanical properties of CuCrZr/316L hybrid components manufactured using selective laser melting, J. Alloys Compd. 955 (2023) 170103, https://doi.org/10.1016/j.jallcom.2023.170103.

[7] R.C. Hugo, R.G. Hoagland, The kinetics of gallium penetration into aluminum grain boundaries—in situ TEM observations and atomistic models, Acta Mater. 48 (2000) 1949–1957, https://doi.org/10.1016/S1359-6454(99)00463-2.

[8] M.H. Razmpoosh, A. Macwan, F. Goodwin, E. Biro, Y. Zhou, Suppression of liquid-metal-embrittlement by twin-induced grain boundary engineering approach, Materialia 11 (2020) 100668, https://doi.org/10.1016/j.mtla.2020.100668.

[9] B. Zhu, J. Lin, Y. Lei, Y. Zhang, Q. Sun, S. Cheng, Additively manufactured δ-ferrite-free 410 stainless steel with desirable performance, Mater. Lett. 293 (2021) 129579, https://doi.org/10.1016/j.matlet.2021.129579.

[10] A. Singh, T. Nath, S.G. Dommeti, S. Sekar, Bulk fabrication of SS410 material using cold metal transfer-based wire arc additive manufacturing process at optimized parameters: microstructural and property evaluation, Machines 10 (2022) 1136, https://doi.org/10.3390/machines10121136.

[11] S. Roy, B. Silwal, A. Nycz, M. Noakes, E. Cakmak, P. Nandwana, Y. Yamamoto, Investigating the effect of different shielding gas mixtures on microstructure and mechanical properties of 410 stainless steel fabricated via large scale additive manufacturing, Addit. Manuf. 38 (2021) 101821, https://doi.org/10.1016/j.addma.2020.101821.

[12] M.M. Amrei, H. Monajati, D. Thibault, Y. Verreman, L. Germain, P. Bocher, Microstructure characterization and hardness distribution of 13Cr4Ni multipass weld metal, Mater. Charact. 111 (2016) 128–136, https://doi.org/10.1016/j.matchar.2015.11.022.

[13] R.J. Moat, A.J. Pinkerton, L. Li, P.J. Withers, M. Preuss, Residual stresses in laser direct metal deposited Waspaloy, Mater. Sci. Eng. A 528 (2011) 2288–2298, https://doi.org/10.1016/j.msea.2010.12.010.

[14] W.F. Savage, Intergranular Attack of Steel by Molten Copper, (n.d.).

[15] E.F. Nippes, D.J. Ball, Copper-Contamination Cracking: Cracking Mechanism and Crack Inhibitors, (n.d.).

[16] C. Dharmendra, S. Shakerin, G.D.J. Ram, M. Mohammadi, Wire-arc additive manufacturing of nickel aluminum bronze/stainless steel hybrid parts – interfacial characterization, prospects, and problems, Materialia 13 (2020) 100834, https://doi.org/10.1016/j.mtla.2020.100834.

[17] K.E. Daehn, A.C. Serrenho, J. Allwood, Preventing wetting between liquid copper and solid steel: a simple extraction technique, Metall. Mater. Trans. B Process Metall. Mater. Process. Sci. 50 (2019) 1637–1651, https://doi.org/10.1007/s11663-019-01578-0.

[18] W.F. Savage, Copper-Contamination Cracking in the Weld Heat-Affected Zone, (n.d.).

[19] D. Sage, C. Fink, Understanding temperature and dwell time dependence of liquid metal embrittlement in austenitic stainless steel by liquid zinc and copper, Materialia 24 (2022) 101502, https://doi.org/10.1016/j.mtla.2022.101502.

[20] B. Barkia, T. Auger, J.L. Courouau, J. Bourgon, Multiscale investigation of crack path and microstructural changes during liquid metal embrittlement of 304L austenitic steel in liquid sodium, Corros. Sci. 127 (2017) 213–221, https://doi.org/10.1016/j.corsci.2017.08.009.

[21] D. Bhattacharya, L. Cho, E. Van Der Aa, H. Ghassemi-Armaki, A. Pichler, K. O. Findley, J.G. Speer, Transgranular cracking in a liquid Zn embrittled high strength steel, Scr. Mater. 175 (2020) 49–54, https://doi.org/10.1016/j.scriptamat.2019.09.006.

[22] A. Legris, G. Nicaise, J.-B. Vogt, J. Foct, Liquid metal embrittlement of the martensitic steel 91: influence of the chemical composition of the liquid metal, J. Nucl. Mater. 301 (2002) 70–76, https://doi.org/10.1016/S0022-3115(01)00730-9.

[23] M.H. Razmpoosh, A. Macwan, F. Goodwin, E. Biro, Y. Zhou, Role of random and coincidence site lattice grain boundaries in liquid metal embrittlement of Iron (FCC)-Zn couple, Metall. Mater. Trans. A 51 (2020) 3938–3944, https://doi.org/10.1007/s11661-020-05857-3.

[24] L. Chen, Study of the relationship between intergranular stress corrosion cracking and grain boundary characteristics in brass, Electrochem. Commun. 131 (2021) 107124, https://doi.org/10.1016/j.elecom.2021.107124.

[25] C.E. Price, R.S. Fredell, A comparative study of the embrittlement of monel 400 at room temperature by hydrogen and by mercury, Metall. Trans. A. 17 (1986) 889–898, https://doi.org/10.1007/BF02643865.